nature photonics

LETTERS

PUBLISHED ONLINE: 18 JANUARY 2016 | DOI: 10.1038/NPHOTON.2015.269

Electro-optic sampling of near-infrared waveforms

Sabine Keiber[1,2], Shawn Sederberg[1], Alexander Schwarz[1], Michael Trubetskov[1,3], Volodymyr Pervak[1,2], Ferenc Krausz[1,2] and Nicholas Karpowicz[1]*

Access to the complete electric field evolution of a laser pulse is essential for attosecond science in general[1], and for the scrutiny and control of electron phenomena in solid-state physics specifically[2–6]. Time-resolved field measurements are routine in the terahertz spectral range, using electro-optic sampling (EOS)[7–9], photoconductive switches[10,11] and field-induced second harmonic generation[12,13]. EOS in particular features outstanding sensitivity and ease of use, making it the basis of time-resolved spectroscopic measurements[14] for studying charge carrier dynamics[15–20] and active optical devices[21]. In this Letter, we show that careful optical filtering allows the bandwidth of this technique to be extended to wavelengths as short as 1.2 μm (230 THz) with half-cycle durations 2.3 times shorter than the sampling pulse. In a proof-of-principle application, we measure the influence of optical parametric amplification (OPA) on the electric field dynamics of a few-cycle near-infrared (NIR) pulse.

As the sampling pulse must usually be shorter than a half-cycle of the field oscillation to be observed, EOS, in which the electric field to be measured induces a polarization change in the sampling pulse, has been constrained to frequencies of 135 THz (2.2 μm) and below[9]. The direct recording of higher-frequency field oscillations has only recently been achieved using the attosecond streaking[22,23] and petahertz optical oscilloscope[24] techniques. These methods exploit the extreme nonlinearities underlying high harmonic generation in gases to induce strong temporal confinement, extending the temporal resolution of few-femtosecond laser pulses to the attosecond timescale. They rely on the generation and detection of extreme ultraviolet radiation, and thus require dedicated vacuum systems, reducing their flexibility and ease of integration with other experiments. An alternative approach is to combine techniques for the characterization of spectral amplitude and phase with carrier envelope phase (CEP) sensitive measurements to extract the complete field[25]. However, simple and direct access to NIR fields is unavailable.

The experimental setup used to demonstrate that EOS can directly provide unambiguous and complete field characterization of a NIR waveform is shown in Fig. 1, and described in detail in Methods. A broadband, phase-stable infrared pulse is generated through difference-frequency generation[26] (DFG), amplified in an optical parametric chirped pulse amplifier (OPCPA) and recombined with a 5-fs sampling pulse with adjustable time delay, after which they are co-focused in a beta barium borate (BBO) crystal. The infrared electric field is sampled via the polarization rotation it induces in the sampling pulse, producing the waveform shown in Fig. 1b. The accuracy of the waveform acquisition is verified by comparing the spectrum obtained by taking the squared modulus of the Fourier transformation of the sampled electric field with one measured independently by a calibrated InGaAs-based grating spectrometer (Ocean Optics NIRQuest 512). The excellent agreement between the spectra measured in the two methods suggests that the electric field is recorded without significant distortions, due to the association between a flat spectral amplitude and flat spectral phase in the response of the process (see Methods for details).

At first glance, this agreement is surprising, given that our 5-fs pulse duration would be expected to introduce a roll-off at approximately 100 THz, with rapidly decreasing sensitivity at higher frequencies as the polarization is rotated in opposite directions by adjacent half-cycles within the pulse, leading to a strongly diminished signal. This somewhat unexpected performance originates in the fact that, as depicted in the inset of Fig. 1a, the mechanism of the polarization rotation in high-frequency (broadband) EOS differs from the standard picture of the quasi-static Pockels effect, where the sampling pulse should be significantly shorter than a half-period of the oscillation to be observed. When sampling a high-frequency waveform, a perpendicularly polarized nonlinear signal is generated that—compared with the sampling pulse—is shifted to higher or lower frequencies in the case of phase-matching of the sum frequency generation (SFG) or DFG, respectively. To produce a polarization rotation, this nonlinearly generated signal should be degenerate with another reference wavelength present in the spectrum of the sampling pulse. We detect SFG in our study, as DFG would have considerable spectral overlap with the pulse we wish to sample.

The detection process requires two steps: first, a sum frequency between the infrared and sampling waves must be generated, and the new wave must then interfere with a local oscillator within the pre-existing sampling spectrum. Accordingly, the frequency response $S(\Omega)$ of EOS is given by

$$S(\Omega) = \int_{\Omega}^{\infty} d\omega_{LO} R(\omega_{LO}) |E(\omega_{LO})| |E(\omega_{LO} - \Omega)| e^{i[\phi(\omega_{LO}) - \phi(\omega_{LO} - \Omega)]} \quad (1)$$

integrating over local oscillator frequencies ω_{LO}, where $|E(\omega)|e^{i\varphi(\omega)}$ represents the complex spectral amplitudes of the sampling pulse, Ω is the frequency of the wave to be sampled and $R(\omega)$ is the response of the detection system.

The shortest wavelengths in the sampling spectrum function as local oscillators for the largest number of detected frequencies. Therefore, emphasizing these components of the pulse favours high-frequency detection. The spectrum of our sampling pulse is shown in Fig. 2—the wavelength region from 600–500 nm has been depleted by DFG, but nonetheless contains non-zero energy. The sampling pulse is transmitted through a short-pass filter with 600 nm cut-off wavelength before the polarization is detected, which firstly improves the signal-to-noise ratio[27] but also, as we will show, dramatically increases the detection bandwidth.

Applying equation (1) to the measured complex spectrum of the sampling pulse, it is found that when $R(\omega) = 1$ the response is substantially reduced above 100 THz, shown in Fig. 2b. However, if

[1]Max-Planck-Institut für Quantenoptik, Hans-Kopfermann-Strasse 1, D-85748 Garching, Germany. [2]Department für Physik, Ludwig-Maximilians-Universität, Am Coulombwall 1, D-85748 Garching, Germany. [3]Research Computing Center, Moscow State University, Leninskie Gory, 119992 Moscow, Russia.
*e-mail: nicholas.karpowicz@mpq.mpg.de

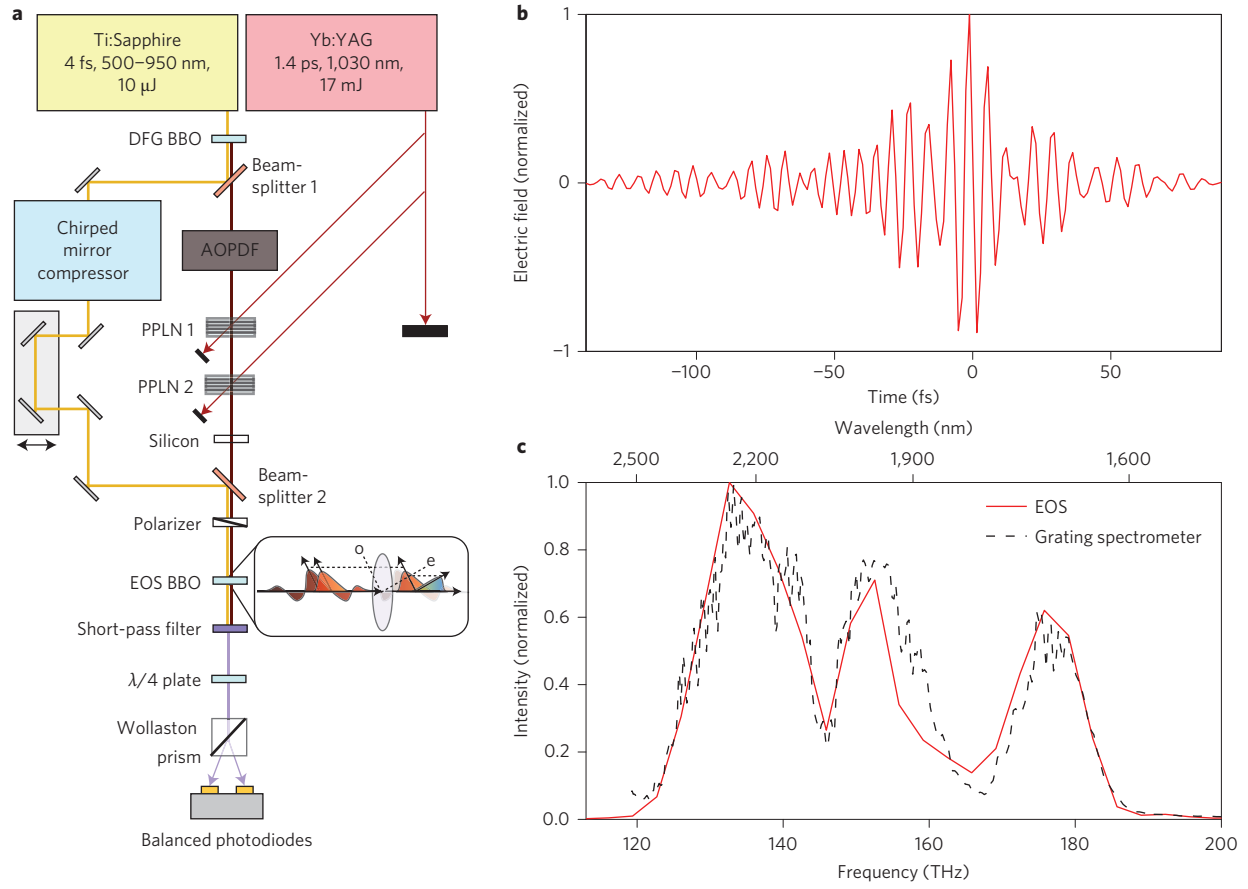

Figure 1 | System layout and representative results. a, The OPCPA and detection scheme, utilizing two optically synchronized laser systems operating at 3 kHz, seeded by the same Ti:Sapphire oscillator. PPLN: periodically poled lithium niobate. Inset, Illustration of the type-I EOS process employed, where the infrared and visible pulses enter the crystal on the ordinary (o) axis and produce a sum-frequency pulse on the extraordinary (e) axis, which has spectral and temporal overlap with the residual visible light on the o axis. **b**, Recorded electric field versus time delay measured via the polarization rotation detected by the Wollaston prism and balanced photodiodes. **c**, Comparison of the Fourier transform of the waveform in (**b**) and the spectrum measured by a calibrated InGaAs-based grating spectrometer.

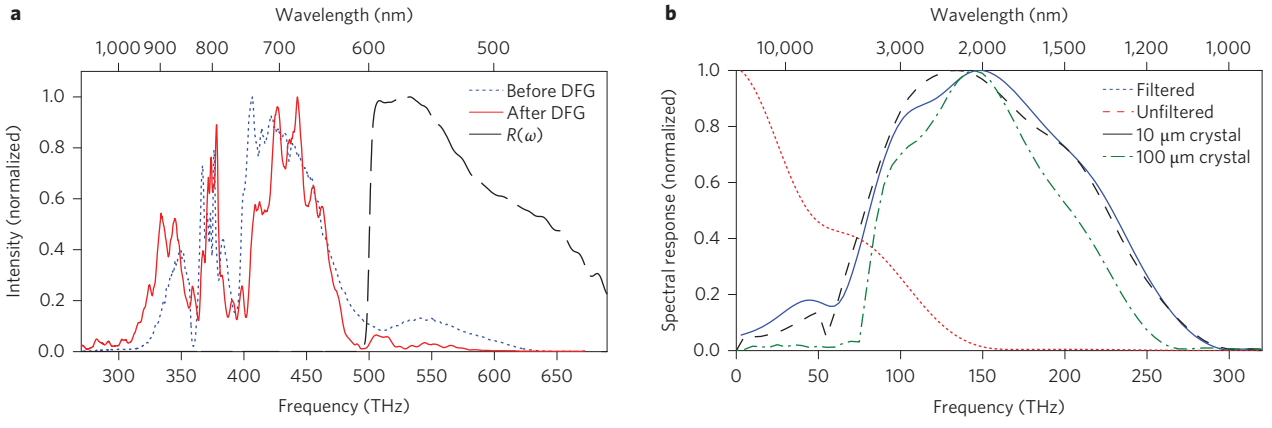

Figure 2 | Sampling pulse spectrum and calculated EOS response functions. a, The sampling pulse undergoes a significant red-shift during the DFG process, creating a depleted region in the spectral range where the detection system is active, with measured response function $R(\omega)$. **b**, The effect of spectral filtering on the spectral response function of EOS using the measured sampling pulse. The 'filtered' curve corresponds to the system employed, including the short-pass filter depicted in (**a**), while the 'unfiltered' curve assumes spectrally uniform detection. Calculations including nonlinear propagation and dispersion in the crystal show similar responses for both 10 and 100 μm crystal thicknesses when the same spectral filter is employed.

the response is recalculated with spectral weights determined by the transmission of the short-pass filter and the response of the silicon photodiodes in the balanced detector, there is a dramatic shift towards higher frequencies, with a peak at 150 THz and FWHM bandwidth over 150 THz. Numerically propagating the infrared and sampling pulses with the nonlinear wave equation through the birefringent crystal shows that this broad bandwidth phase-matches well in BBO, with the spectral width only slightly

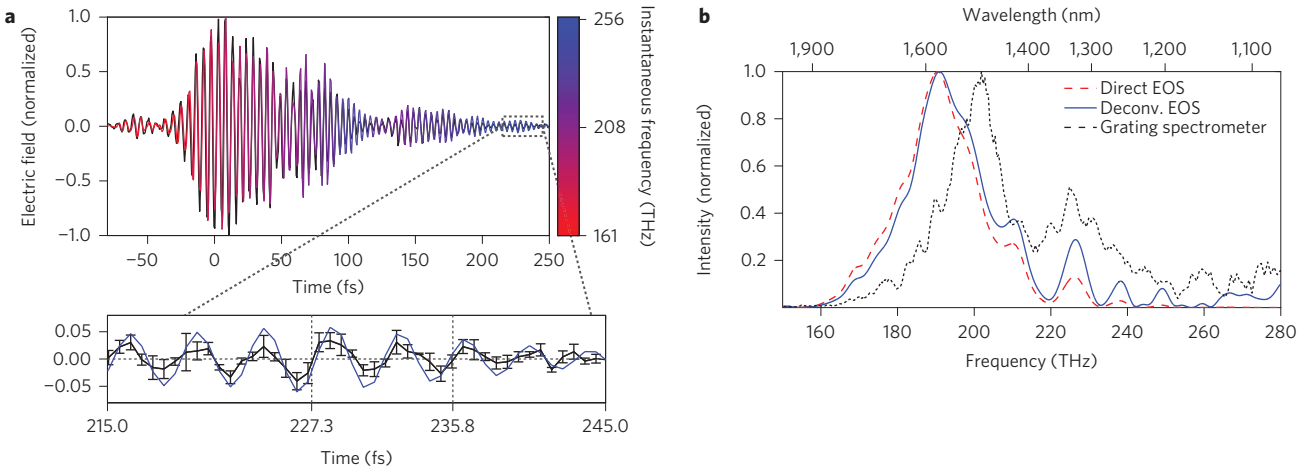

Figure 3 | Sampling of high-frequency NIR light. a, Waveform measured with AOPDF removed and DFG phase-matching set to short wavelengths, chirped in silicon wafer. The colour of the line portrays the instantaneous frequency of the wave. The black line shows the raw data without filtered deconvolution. Inset, Zoomed-in view of high-frequency oscillations at the trailing edge of pulse, with zero crossings two periods apart marked, exhibiting 4.25 fs period corresponding to 1.27 μm, or 235 THz. Error bars indicate the standard error of the mean of four consecutive measurements. **b**, Spectrum measured with EOS compared with that measured with InGaAs-based grating spectrometer, both with and without correction for calculated spectral response.

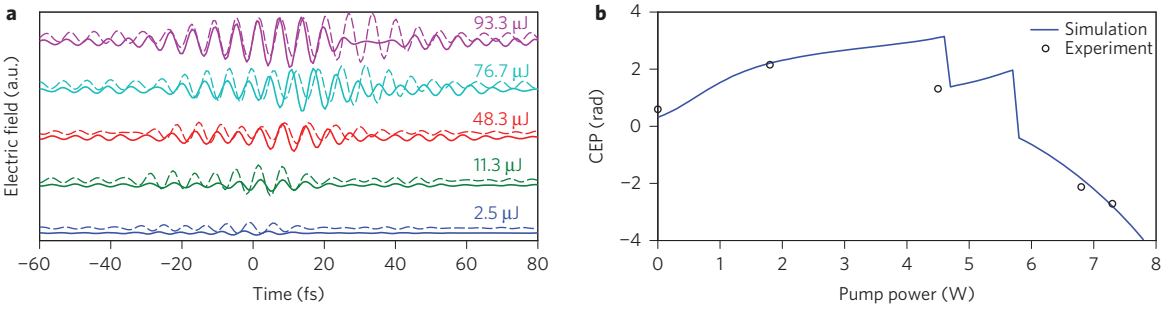

Figure 4 | OPCPA pulse amplification dynamics measured with EOS. a, Waveforms corresponding to (from top to bottom) pump powers of 7.3, 6.8, 4.5, 1.8 and 0 W in second OPCPA stage, corresponding to amplified pulse energies of 93.3, 76.6, 48.3, 11.3 and 2.5 μJ, respectively. Dashed lines are simulated waveforms. Waveforms are offset for clarity. **b**, CEP change versus pump power: black circles are measured values, blue line is simulated relation. Jumps in the simulated curve are due to pulse envelope reshaping causing a change in which oscillation peak has the greatest amplitude.

reduced in a 100-μm-thick crystal, as plotted in Fig. 2b. Therefore, this scheme allows for unattenuated detection of the whole OPA bandwidth and significantly extends the cut-off frequency. We note that this is only the case when the signal contributions of all local oscillators add coherently, requiring that the spectral components in the pulse involved in the detection process, the local oscillators themselves and the lower-frequency mixing inputs, have minimal group delay dispersion.

We tested the spectral limits of EOS with 5-fs sampling pulses by tuning the phase-matching of the DFG BBO crystal to generate a phase-stable NIR continuum favouring shorter wavelengths, and bypassing the OPA due to its limited transmission bandwidth. A positive chirp was applied to the pulse such that its spectral components were clearly separated in time, with faster oscillations appearing at the trailing edge. Owing to the large dynamic range provided by the filtered and balanced detection scheme (on the order of 10^5 in the case of the amplified pulse), this unamplified and temporally stretched field with energies on the tens of nanojoules scale is nonetheless easily detectable, as shown in Fig. 3. Characterization of the sampling pulse spectral phase by cross-correlation frequency-resolved optical gating (XFROG, see Methods), $\phi(\omega)$, enabled filtered deconvolution from the EOS response function. Cycles with 4.25 fs period are clearly visible in both the deconvolved and raw measurement, as marked in the zoomed-in area, corresponding to a half-cycle duration 2.3 times shorter than the sampling pulse duration. Detected wavelengths reach 1.2 μm, visible on a linear scale after Fourier transformation directly performed on the raw data, exhibiting good agreement with the spectrum measured with the grating spectrometer after deconvolution.

The ability to directly record NIR waveforms without the involvement of XUV radiation and complex vacuum apparatus presents numerous opportunities in both fundamental science and applied optical research. To demonstrate the ability of the technique to observe technologically relevant and complicated phenomena, we apply it to the OPA process itself, as pulses are amplified by nearly two orders of magnitude, from 2.5 to 93 μJ. In this scenario, the large dynamic range and absolute field information enable the study of the influence of the amplification process on the CEP. In Fig. 4, the significant changes in the amplified waveform indicate the complexity of the cascaded nonlinear optical process, especially as it saturates (at a pump power of 7.3 W in our case). A temporal shift and reshaping of the waveform are seen as it is amplified. This is due to a combination of the OPA phase[28] and the thermo-optic effect inside of the lithium niobate crystal. Most importantly for applications where CEP stability is paramount, the CEP changes significantly with pump power, over a 5-radian span as confirmed by simulations of nonlinear pulse propagation inside the crystal and subsequent linear propagation and focusing of the pulse (described in further detail in the Methods). This strong coupling between phase and pump power in a single OPA stage emphasizes

the necessity of extreme pump laser stability for phase-dependent experiments relying on multi-stage OPA systems. The non-monotonic CEP dynamics present a possible means of CEP management, by setting the phase shift of multiple amplification stages such that positive and negative slopes of phase versus power nullify the net phase shift from fluctuations in pump power.

In summary, EOS is a powerful technique in the NIR, giving access to the temporal evolution of electric fields covering the entire telecommunications band with a single, coherent measurement in free-space, without retrieval algorithm or complex data processing. Access to the exact waveform, including spectral amplitude, spectral phase and absolute CEP, of few-cycle mid-to-near-infrared lasers will be an essential tool for the next generation of attosecond and strong-field physics measurements making use of the rising availability of reliable sources in this spectral range by allowing for direct comparison of the applied electric field in experiment and theory.

Methods

Methods and any associated references are available in the online version of the paper.

Received 15 August 2015; accepted 9 December 2015; published online 18 January 2016

References

1. Krausz, F. & Ivanov, M. Attosecond physics. *Rev. Mod. Phys.* **81,** 163–234 (2009).
2. Hohenleutner, M. *et al.* Real-time observation of interfering crystal electrons in high-harmonic generation. *Nature* **572,** 572–575 (2015).
3. Schultze, M. *et al.* Controlling dielectrics with the electric field of light. *Nature* **493,** 75–78 (2013).
4. Kuehn, W. *et al.* Coherent ballistic motion of electrons in a periodic potential. *Phys. Rev. Lett.* **104,** 146602 (2010).
5. Eisele, M. *et al.* Ultrafast multi-terahertz nano-spectroscopy with sub-cycle temporal resolution. *Nature Photon.* **8,** 841–845 (2014).
6. Schubert, O. *et al.* Sub-cycle control of terahertz high-harmonic generation by dynamical Bloch oscillations. *Nature Photon.* **8,** 119–123 (2014).
7. Wu, Q. & Zhang, X.-C. Free-space electro-optic sampling of terahertz beams. *Appl. Phys. Lett.* **67,** 3523–3525 (1995).
8. Leitenstorfer, A., Hunsche, S., Shah, J., Nuss, M. C. & Knox, W. H. Detectors and sources for ultrabroadband electro-optic sampling: experiment and theory. *Appl. Phys. Lett.* **74,** 1516–1518 (1999).
9. Sell, A., Scheu, R., Leitenstorfer, A. & Huber, R. Field-resolved detection of phase-locked infrared transients from a compact Er:fiber system tunable between 55 and 107 THz. *Appl. Phys. Lett.* **93,** 251107 (2008).
10. Auston, D. H., Cheung, K. P. & Smith, P. R. Picosecond photoconducting Hertzian dipoles. *Appl. Phys. Lett.* **45,** 284–286 (1984).
11. Ashida, M. Ultra-broadband terahertz wave detection using photoconductive antenna. *Japan. J. Appl. Phys.* **47,** 8221–8225 (2008).
12. Dai, J., Xie, X. & Zhang, X.-C. Detection of broadband terahertz waves with a laser-induced plasma in gases. *Phys. Rev. Lett.* **97,** 103903 (2006).
13. Karpowicz, N. *et al.* Coherent heterodyne time-domain spectrometry covering the entire 'terahertz gap'. *Appl. Phys. Lett.* **92,** 011131 (2008).
14. Pashkin, A. *et al.* Femtosecond response of quasiparticles and phonons in superconducting $YBa_2Cu_3O_7$ studied by wideband terahertz spectroscopy. *Phys. Rev. Lett.* **105,** 067001 (2010).
15. Waschke, C. *et al.* Coherent submillimeter-wave emission from Bloch oscillations in a semiconductor superlattice. *Phys. Rev. Lett.* **70,** 3319–3322 (1993).
16. Gaal, P. *et al.* Internal motions of a quasiparticle governing its ultrafast nonlinear response. *Nature* **450,** 1210–1213 (2007).
17. Kübler, C. *et al.* Coherent structural dynamics and electronic correlations during an ultrafast insulator-to-metal phase transition in VO_2. *Phys. Rev. Lett.* **99,** 116401 (2007).
18. Somma, C., Reimann, K., Flytzanis, C., Elsaesser, T. & Woerner, M. High-field terahertz bulk photovoltaic effect in lithium niobate. *Phys. Rev. Lett.* **112,** 146602 (2014).
19. Pashkin, A., Sell, A., Kampfrath, T. & Huber, R. Electric and magnetic terahertz nonlinearities resolved on the sub-cycle scale. *New J. Phys.* **15,** 065003 (2013).
20. Huber, R. *et al.* How many-particle interactions develop after ultrafast excitation of an electron-hole plasma. *Nature* **414,** 286–289 (2001).
21. Kröll, J. *et al.* Phase-resolved measurements of stimulated emission in a laser. *Nature* **449,** 698–701 (2007).
22. Itatani, J. *et al.* Attosecond streak camera. *Phys. Rev. Lett.* **88,** 173903 (2002).
23. Goulielmakis, E. *et al.* Direct measurement of light waves. *Science* **305,** 1267–1269 (2004).
24. Kim, K. T. el al. Petahertz optical oscilloscope. *Nature Photon.* **7,** 958–962 (2013).
25. Nomura, T., Shirai, H. & Fuji, T. Frequency-resolved optical gating capable of carrier-envelope phase determination. *Nature Commun.* **4,** 2820 (2013).
26. Fattahi, H., Schwarz, A., Keiber, S. & Karpowicz, N. Efficient, octave-spanning difference-frequency generation using few-cycle pulses in simple collinear geometry. *Opt. Lett.* **38,** 4216–4218 (2013).
27. Porer, M., Ménard, J.-M. & Huber, R. Shot noise reduced terahertz detection via spectrally postfiltered electro-optic sampling. *Opt. Lett.* **39,** 2435–2438 (2014).
28. Demmler, S. *et al.* Control of nonlinear spectral phase induced by ultra-broadband optical parametric amplification. *Opt. Lett.* **37,** 3933–3935 (2012).

Acknowledgements

We acknowledge support from LASERLAB-EUROPE (grant agreement no. 284464, the European Commission's Seventh Framework Programme) and the Munich-Centre for Advanced Photonics. S.S. acknowledges financial support from the Banting Postdoctoral Fellowship program.

Author contributions

The measurement was performed by S.K., S.S. and N.K. The OPCPA was prepared by A.S., S.K., F.K. and N.K. The specialized multilayer optics were designed and fabricated by M.T. and V.P. The simulations were performed by and the experimental concept was conceived by N.K. All authors reviewed and contributed to the final manuscript.

Additional information

Supplementary information is available in the online version of the paper. Reprints and permissions information is available online at www.nature.com/reprints. Correspondence and requests for materials should be addressed to N.K.

Competing financial interests

The authors declare no competing financial interests.

Methods

Optical system. The sampled infrared waveforms are derived from a two-stage OPCPA with a central wavelength of 2.1 μm, operating at 3 kHz repetition rate[29]. The seed for the OPCPA is generated by focusing a 4-fs white-light pulse into a 500 μm thick type-II BBO crystal (Castech) for intrapulse DFG. The unconverted white light is separated with a dichroic beamsplitter, recompressed with a chirped mirror compressor, and reused as the sampling pulse in the EOS setup. The final white light pulse duration is measured to be 5 fs using XFROG, with measured spectrogram and waveform shown in Supplementary Fig. 1.

The spectral phase of the passively phase-stable infrared seed pulses is shaped in an acousto-optic programmable dispersive filter (AOPDF) (DAZZLER, Fastlite) and amplified via two OPCPA stages in 5% MgO-doped periodically poled lithium niobate (PPLN) crystals with 2 and 1 mm thicknesses for the first and second stage, respectively. The stages are pumped by a thin-disk Yb:YAG regenerative amplifier[30] with 0.4 and 3 mJ pulse energy, respectively. 4 mm of silicon are used to compress the 100 μJ infrared pulses below two optical cycles (13 fs).

The white light sampling and infrared pulses are recombined collinearly with a dichroic beamsplitter, and focused into a type-I BBO crystal (Innowit) for electro-optic sampling. Typical focus sizes are 80 and 180 μm ($1/e^2$) for sampling and sampled pulse, respectively. The polarization rotation imprinted on the sampling pulse is recorded by a balanced photodiode and read out by a lock-in amplifier as a function of delay between the two pulses. Modulation of the CEP with the AOPDF at the lock-in reference frequency allows for heterodyne detection by introducing a shift of the frequency comb of the infrared light. The waveform measurements were performed with a 50-μm-thick BBO in Fig. 1, 15-μm-thick BBO in Fig. 2, and 100-μm-thick BBO in Fig. 3.

Measurement time and dynamic range. A typical acquisition with 150 and 300 laser shots averaged per data point takes about ten minutes. The dynamic range is on the order of $>10^5$ in the electric field.

Measurement of unamplified, broadband continuum. In the case of the measurement of the short-wavelength pulse (Fig. 3), the AOPDF and PPLN amplification stages were removed because of their limited transmission bandwidth and the frequency modulation the AOPDF supplied was replaced with an amplitude modulation via an optical chopper. The slight discrepancy between the spectrum retrieved from EOS and the one measured with the grating spectrometer might stem from the slightly different spectral distributions in the focus that are probed by the EOS and the collimated beam. In the amplified infrared pulse this deviation is less pronounced due to mode filtering by the OPA stages.

Thermal effects in OPCPA crystals. We confirmed a temperature increase of 20 K in the second-stage crystal with a thermal camera as the pump power was increased to 7.3 W leading to the thermo-optic effect contributing to a temporal shift in the amplified waveforms in Fig. 4a.

Simulation of amplification and detection. The simulations are based on the nonlinear wave equation in the slowly-varying amplitude approximation[31] with no assumptions regarding the shape of the pulse envelope, expressed in the frequency domain as

$$\frac{\partial E_\omega(z)}{\partial z} = -ik_\omega E_\omega(z) - \frac{i\omega}{2n(\omega)\varepsilon_o c} P_\omega^{(NL)}(z)$$

where E_ω is the complex amplitude of an individual spectral component, assumed to be a plane wave with wave-vector k_ω propagating in the z direction in a given polarization axis, and $P_\omega^{(NL)}$ is the nonlinear polarization of the crystal on that axis, which is calculated in the time domain via inverse Fourier transformation, and then transformed back to obtain its individual frequency components. The refractive index $n(\omega)$ is frequency dependent, using the dispersion of BBO[32] and $LiNbO_3$[33] in the calculations of EOS and OPCPA, respectively. The propagation scheme is a one-dimensional exponential midpoint algorithm, and considers the birefringence of the crystal, tensor nature of the second order nonlinearity, Kerr effect and thermo-optic effect in the case of $LiNbO_3$. In the OPCPA simulations, a Gaussian spatial profile was assumed for the seed and pump (with 1D simulations performed for each point along the radial coordinate), and the resulting beam propagated in free space with the assumption of radial symmetry and sampled in the centre of the focus of a 200 mm focal length parabolic mirror. The CEP is calculated as the temporal phase at the temporal position of the maximum modulus of the complex analytic waveform.

Phase response of EOS. The response function $S(\Omega)$ is complex-valued. In Supplementary Fig. 2, both the phase and modulus are plotted, considering phase-matching, for 10 and 100 μm crystal thickness. The spectral phase response shows little variation within the FWHM of the spectral amplitude response, in both cases.

References

29. Deng, Y. *et al.* Carrier-envelope-phase-stable, 1.2 mJ, 1.5 cycle laser pulses at 2.1 μm. *Opt. Lett.* **37,** 4973–4975 (2012).
30. Metzger, T. *et al.* High-repetition-rate picosecond pump laser based on a Yb:YAG disk amplifier for optical parametric amplification. *Opt. Lett.* **34,** 2123–2125 (2009).
31. Brabec, T. & Krausz, F. Nonlinear optical pulse propagation in the single-cycle regime. *Phys. Rev. Lett.* **78,** 3282–3285 (1997).
32. Zhang, D., Kong, Y. & Zhang, J. Optical parametric properties of 532-nm-pumped beta-barium-borate near the infrared absorption edge. *Opt. Commun.* **184,** 485–491 (2000).
33. Gayer, O., Sacks, Z., Galun, E. & Arie, A. Temperature and wavelength dependent refractive index equations for MgO-doped congruent and stoichiometric $LiNbO_3$. *Appl. Phys. B* **91,** 343–348 (2008).